

BIMODAL MORPHOLOGY TRANSITION MECHANISM IN THE SYNTHESIS  
OF TWO DIFFERENT SILICA NANOPARTICLES

A Thesis

Presented to the Faculty of the Graduate School

of Cornell University

in Partial Fulfillment of the Requirements for the Degree of

Master of Science

by

Melik Ziya Turker

August 2015

© 2015 Melik Ziya Turker

ALL RIGHTS RESERVED

## ABSTRACT

Morphology transitions in the surfactant directed synthesis of mesoporous silica nanoparticles are of great interest as these materials are interesting for applications in catalysis, separation, and drug delivery. The nature of the transition mechanisms often remains unknown, but is vital to understanding of better-designed materials. We investigate a bimodal transition mechanism in the synthesis of single pore silica nanoparticles of two different shapes synthesized through micelle templating. Introducing pore expander trimethylbenzene (TMB) to the system at varying concentrations results in a transition from pure thicker single-pore particles to pure thinner single-pore particles. In the transition region both particles have stable pore and particle sizes while after the transition region an increase in the size of the thinner particles is observed. The bimodal nature of the transition is verified by a combination of gel permeation chromatography (GPC), fluorescence correlation spectroscopy (FCS), dynamic light scattering (DLS) and transmission electron microscopy (TEM) techniques.

## BIOGRAPHICAL SKETCH

Melik Turker was born and raised in Trabzon, Turkey. He graduated from the Department of Metallurgical and Materials Engineering at Istanbul Technical University (ITU) in 2012. Melik arrived at Cornell University in 2013, and joined the research group of Professor Ulrich Wiesner. He focused on fluorescent silica nanoparticles for cancer diagnosis and treatment, and he graduated from the Master of Science program of Materials Science and Engineering Department at Cornell University in 2015.

*Dedicated to the memory of*

*My Grandfather*

## ACKNOWLEDGEMENTS

I would first like to thank my parents and family for their support in my education and their trust in me. I would like to thank Professor Uli Wiesner for his excellent guidance, endless support, and sincere relationship in which I found the enthusiasm to conduct my research without boundaries in a wonderful research environment in Ithaca. I also thank my committee member Professor Lara Estroff for her guidance and kind help.

I would like to thank all the Wiesner Group members, especially Kai, Teresa, Ferdinand and Yao for their help and company in the laboratory. I would also like to express my gratitude to all the staff members at Cornell, specifically Dolores Dewbury and Michele Conrad from Cornell MSE, Penny Burke from NBTC and John Grazul from CNF. I would like to express my sincere thanks to Professor Mustafa Urgan, Professor Nuri Solak, Professor Devrim B. Kaymak, Professor Eyup S. Kayali from ITU, and Professor Orhan Aydin and Professor Mehmet Akbas from KTU. I would also like to thank Dr. Aksit, Dr. Ahsan, Mr. Gunceler, Mr. Bilgen and many of the great people, who were always supportive to me and whom I always enjoyed their lifelong friendship. I also thank the Republic of Turkey for the financial support in my studies.

## TABLE OF CONTENTS

Biographical Sketch	iv
Dedication	v
Acknowledgements	vi
Table of Contents	vii
List of Figures	viii
<b>CHAPTER 1</b>	<b>1</b>
INTRODUCTION	1
1.1 Mesoporous Silica Nanoparticles	1
1.2 Organization of the Thesis	3
<b>CHAPTER 2</b>	<b>4</b>
MATERIALS AND METHODS USED TO SYNTHESIZE MC-DOTS AND C-RINGS	4
2.1 Materials	4
2.2 Methods	5
2.2.1 Synthesis of the Particles	5
2.2.2 Purification of the Particles	6
2.2.3 Analysis of GPC Curves	6
2.2.4 Characterization of Particle Morphology and Size	8
2.2.5 Characterization of Fluorescent Properties of mC- Dots and C-Rings	9
<b>CHAPTER 3</b>	<b>10</b>
RESULTS AND DISCUSSION	10
<b>CHAPTER 4</b>	<b>19</b>
CONCLUSION	19
<b>CHAPTER 5</b>	<b>20</b>
SUPPLEMENTAL MATERIALS	20
REFERENCES	28

## LIST OF FIGURES

Fig. 3.1:	Illustration of bimodal transition and mC-Dots and C-Rings morphologies.....	10
Fig. 3.2:	Change in the hydrodynamic diameter of samples at varying TMB concentrations, measured by FCS.....	12
Fig. 3.3:	TEM images of samples at varying TMB concentrations.....	13
Fig. 3.4:	Gaussian distributions for the GPC curves of samples with varying TMB concentrations.....	14
Fig. 3.5:	Populations ratios of mC-Dots and C-Rings and skewness calculated by GPC curves, population and size analysis by TEM.....	16
Fig. 5.1:	GPC results of the samples with varying TMB concentrations.....	20
Fig. 5.2:	Change in the hydrodynamic diameter of samples at varying TMB:CTAB molar ratios, measured by DLS .....	21
Fig. 5.3:	Effect of varying TMB concentrations on hydrodynamic C-Rings size in growth region, measured by FCS and DLS.....	22
Fig. 5.4:	TEM image of 43.3 mM TMB sample in transition region showing mC-Dots darker and C-Rings dimmer on TEM grid due to the three and one dimensional particle morphologies.....	22
Fig. 5.5:	Comparison of population ratios of mC-Dots and C-Rings derived from TEM and FCS measurements.....	23
Fig. 5.6:	Population and size analysis of 0 mM TMB sample on TEM images .....	24

Fig. 5.7:	Population and size analysis of 72.17 mM TMB sample on TEM images.....	25
Fig. 5.8:	Population and size analysis of 14.43 mM TMB sample on TEM images.....	26
Fig. 5.9:	Population and size analysis of 21.65 mM TMB sample on TEM images.....	27

# CHAPTER 1

## INTRODUCTION

### 1.1 Mesoporous Silica Nanoparticles

Discovery of MCM-41 materials (1992) with pore sizes  $\sim 15\text{-}100$  Å has brought attention to the formation mechanism of Mesoporous Silica Nanoparticles (MSNs) synthesized through the interaction of silica and micelles.<sup>1,2</sup> MSNs have found many applications such as drug delivery and biosensor materials.<sup>28,29,30,31,32,33</sup>

The development of SBA-15 materials (1998) with larger pore sizes (46-300 Å) by the addition of oil phase, and their phase transformation mechanisms from hexagonally ordered SBA-15 silicas to Mesocellular Foams (MCFs) has paved the way on MSNs research.<sup>3,4</sup> In 2000, Stucky et al. showed that adding sufficient 1,3,5-trimethylbenzene (TMB) not only leads an increase in the pore size of SBA-15 silicas, but also causes a phase transformation from highly ordered SBA-15 silicas to disordered MCFs.<sup>5</sup> Hexagonally ordered SBA-15 silicas with pore sizes 4-12 nm transforms into MCFs ( pore sizes 22-42 nm).<sup>6</sup> While MCFs form through spherical micelle templates,<sup>6</sup> SBA-15 silicas form through cylindrical templates which start out as spheres and go through a morphological change upon the addition of tetraethyl orthosilicate (TEOS) which screens the charge and repulsive interaction between micelle head groups.<sup>6,8,9</sup> The addition of TEOS turns micelles into cylindrical rods to decrease the effective area which micelle head

\*This work was conducted in Wiesner Research Group with the TEM and DLS data contribution of Kai Ma.

groups occupy.<sup>6,8,9</sup> By the addition of TMB, rod-like templates turn into noded micelle structure (spheres) to reduce the surface to volume ratio by covering oil droplets with minimum amount of polymer.<sup>6</sup> Afterwards, for MCF formation, the size of the micelles increases until the micelle cores saturate with TMB, which results in the formation of aggregated spherical micelles.<sup>6,10,11,19</sup> In 2015, Wang et al. stated that the ordered structure of SBA-15 silicas is only maintained for low TMB concentrations ( $\text{TMB/surfactant}:2$ ). Phase transformation to spherical micelles occurs at high TMB concentrations resulting in larger pore sizes.<sup>7</sup>

It was also stated that TMB molecules might occupy the micelle surfaces through  $\pi$ -cation interactions of surfactant head groups and oil molecules at low oil concentrations.<sup>12,13,14,15</sup> TMB molecules preferentially occupy cores of the micelles above saturation of TMB on micelle surfaces.<sup>24</sup> Excess amounts of TMB swells the cores of micelles until the saturation of micelle interiors with TMB, resulting in maximum micelle size.<sup>24</sup>

The tunable nature of MSNs brought attention to the possibility of cancer diagnosis and treatment by silica nanoparticles (SNPs).<sup>17,20,21</sup> The Wiesner Group at Cornell developed FDA-approved fluorescent SNPs, called C-Dots for clinical cancer investigations.<sup>18,25</sup> Promising human trials led to the research focusing on cancer treatment in addition to cancer diagnostics. Mesoporous Cornell Dots (mC-Dots) developed by Ma et. al. in water synthesis using TMOS as silica precursor, instead of conventional Stöber synthesis made it possible to control particle morphology and size below 10 nm.<sup>18,20,24</sup> TMOS with a fast hydrolysis rate in water provides a better morphology control than TEOS that has a slower hydrolysis rate. In addition, the use of cationic surfactant ( $\text{C}_{16}\text{TAB}$ ) templates the silica condensation.<sup>16,18,20,22</sup> In 2015, Ma et. al.

investigated the use of TMB in mC-Dots synthesis and developed torus shaped fluorescent silica nanoparticle called C-Rings, which has a larger pore size than mC-Dots.<sup>21</sup>

The study of pore sizes and morphology transitions of MSNs have always been a curiosity, since the discovery of MCM-41 materials. There have been number of studies trying to exceed size limits of MSNs and focusing on their different phases, but the detailed nature of the morphology transitions remains unknown.<sup>1,2,3,4,5,6</sup>

Here, we represent a bimodal morphology transition between mC-Dots and C-Rings synthesized through an oil/surfactant templated mechanism with varying TMB concentrations. This study reveals the nature of a morphology transition for oil/surfactant/silica system and gives insight to oil/surfactant interactions, which could lead to the discovery of new material types allowing for new applications in the future.

## **1.2 Organization of the Thesis**

We have tried to show the bimodal transition phenomena through the thesis. In the first part of the thesis, we have reviewed the related literature. In Chapter 2, we have explained the experimental background of this work. In Chapter 3 and 4, results, discussion and conclusion of this work were stated. Chapter 5 includes the supplementary figures of this study.

## CHAPTER 2

### MATERIALS AND METHODS USED TO FABRICATE MC-DOTS AND C-RINGS

#### 2.1 Materials

All materials were used as received. Hexadecyltrimethyl ammonium bromide (CTAB,  $\geq 99\%$ ), tetramethyl orthosilicate (TMOS,  $\geq 99\%$ ), 2.0 M ammonium hydroxide in ethanol, and anhydrous dimethyl sulfoxide (DMSO,  $\geq 99\%$ ) were purchased from Sigma Aldrich. 2-[methoxy(polyethyleneoxy)6-9propyl]trimethoxysilane (PEG-Silane, MW.  $\sim 500$ ), and (3-mercaptopropyl) trimethoxysilane (MPTMS, 95%) were obtained from Gelest. Mesitylene (TMB, 99% extra pure) was purchased from Acros Organics. Tetramethylrhodamine-6 C2 maleimide (TMR) was purchased from Anaspec. Absolute anhydrous ethanol (200 proof) was obtained from Pharmco-Aaper. Glacial acetic acid was purchased from Macron Fine Chemicals. 0.9% sodium chloride irrigation USP solution was purchased from Braun. Syringe filters (0.2  $\mu\text{m}$ , PTFE membrane) were purchased from VWR International. Vivaspin sample concentrators (MWCO 30K) and Superdex 200 prep grade were obtained from GE Health Care. Snake skin dialysis membrane (MWCO 10K) was purchased from Life Technologies. Deionized (DI) water was generated using Millipore Milli-Q system (18.2 M $\Omega$ .cm).

## 2.2 Methods

### 2.2.1 Synthesis of the Particles

MC-Dots and C-Rings were synthesized as described in the literature.<sup>17,20,21</sup> 0.227 mmol of CTAB and 1 mL of 20 mM aqueous ammonium hydroxide solution were added into 9 mL DI water. There was no addition of TMB following this step for the synthesis of mC-Dots, whereas the concentration of TMB was varied from 14.4 mM to 360.8 mM to form C-Rings with different diameters. Then the solution was stirred for 40 min at 30 °C to fully dissolve CTAB. Following that, 0.45 mmol TMOS, and 0.0004 mmol TMR dye (conjugated 12 h prior to addition with 0.01 mmol MPTMS in DMSO) were added into the reaction under stirring. Afterwards, the solution was kept stirred at 30 °C for 24 h. After that, 0.21 mmol PEG-silane was added into the solution and stirring continued for another 24 h at 30 °C to quench the particle growth. Then, the sample was heated at 80 °C for 24 h without stirring to covalently attach the PEG-silane functional groups onto SNP surface.

In the next step, the solution was cooled down to room temperature and subsequently transferred into a dialysis membrane. After that, the sample solution was dialyzed for 24 h to extract CTAB and TMB out of the pores in a 200 mL acid solution, which is a mixture of ethanol, DI water and acetic acid (volume ratio 1:1:0.014). This step was repeated three times and followed by dialysis in 2 L DI water for 24 h, which was also repeated 3 times. Subsequently, the sample solution was syringe filtered (0.2 µm MWCO) to remove aggregates. The relative molar ratios of the reactants

were 1 TMOS: 0.498 CTAB: 0.043 ammonium hydroxide: (0 – 7.89) TMB: 0.47 PEG-Silane: 0.00088 TMR: 0.022 MPTMS: 1090.9 DI water.

## **2.2.2 Purification of the Particles**

Following the dialysis step, samples were transferred into spin filter sample concentrators and centrifugation (Eppendorf 5810 R) was performed at 4300 RPM for 30 min. After that, 400  $\mu$ L of up-concentrated samples were injected into GPC column packed by Superdex 200 prep grade resin. Buffer solution (0.9% sodium chloride) was pumped into the column by Bio-Rad BioLogic LP system. Bio-Rad BioFrac fraction collector collected GPC fractions of samples. Following the fractionation, particles were separated from aggregates and free dyes, and transferred back into spin filters. Following the centrifugation at 4300 RPM for 30 min for 3 times, particles were syringe filtered for characterization.

## **2.2.3 Analysis of GPC Curves**

Bio-Rad LP data view software recorded ultraviolet (UV) intensity – time graphs for each sample. Software was employed to fit two Gaussian distribution into one-peaked curves. Peak centers for the two distributions were floated to see if the software still gives the same distribution fits. Areas below each fit were compared to calculate the ratio between mC-Dots and C-Rings populations.

Aggregation and free dye intensity peaks were ignored by only selecting the main peaks highlighted in red color for skewness calculations (Figure 5.1). Skewness is the division of the third moment by the cube of standard deviation.<sup>26</sup> Since probability for each data point is not equal to each other, each data point was weighted by  $\frac{y_j}{\sum_i y_i}$ , where y-axis is UV intensity. Average time is defined as

$$X_{ave} = \sum_{ij} X_j \times \frac{y_j}{\sum_i y_i} \quad (2.1)$$

where x is the time axis. Second moment is

$$2^{nd} \text{ moment} = \sum_{ij} \left( (X_j - X_{ave})^2 \times \frac{y_j}{\sum_i y_i} \right) \quad (2.2)$$

Standard deviation is defined as

$$\text{Standard Deviation} = \sqrt{2^{nd} \text{ moment}} \quad (2.3)$$

Third moment is expressed as

$$3^{rd} \text{ moment} = \sum_{ij} \left( (X_j - X_{ave})^3 \times \frac{y_j}{\sum_i y_i} \right) \quad (2.4)$$

Finally skewness is calculated by the formula

$$Skewness = \frac{3^{rd} \text{ moment}}{Standard \ Deviation^3} \quad (2.5)$$

## 2.2.4 Characterization of Particle Morphology and Size

For TEM sample preparation, 1  $\mu\text{L}$  of each sample were diluted into 100  $\mu\text{L}$  ethanol, and 10  $\mu\text{L}$  of this solution were dropped onto TEM grids and ethanol was evaporated at room temperature. Transmission electron microscopy (TEM) images were taken using a FEI Tecnai T12 Spirit model microscope operated with an acceleration voltage of 120 kV. In order to analyze particle morphology and size distribution from TEM images, we manually drew blue filled circles for mC-dots and red filled circles for C-Rings over hundreds of particles for each sample (Figure 5.6-9). Manually processed images were exported to ImageJ software. MC-Dots and C-Rings were differentiated from their three and one-dimensional morphologies. First, we split blue and red color channels of image for processing. Then, each channel was filtered by thresholding. After that, each processed image was split into 4 equal pieces for error calculation. In the last step, software calculated the particle numbers and average areas for each population. Particle diameters were calculated by the square root of the average areas. The ratios between mC-Dots and C-Rings populations were calculated by comparing the numbers of particles.

Hydrodynamic particle sizes and size distributions by number were measured by dynamic light scattering (DLS) technique performed on Malvern Zetasizer Nano-ZS operated at 20  $^{\circ}\text{C}$ . Measurements were repeated for 3 times in DI water for each sample to average the sample size.

## **2.2.5 Characterization of Fluorescent Properties of mC-Dots and C-rings**

All of the samples and free dye were absorption matched by dilution into DI water. Varian Cary 5000 spectrophotometer (Varian, Inc., Palo Alto, CA) was employed to measure and match the absorption spectra of each sample. Extinction coefficient of TMR ( $88000 \text{ M}^{-1} \text{ cm}^{-1}$ ) was used to calculate the concentration of dyes encapsulated in the samples.

Emission spectrums of absorption-matched samples were measured by Photon Technologies International Quantamaster spectrofluorometer (PTI, Birmingham, NJ) to approximate the quantum efficiency relative to free dye.

Fluorescence correlation spectroscopy (FCS) measurements were performed on a home-built FCS setup using HeNe 535 nm laser excitation source to obtain hydrodynamic size, brightness per particle and concentration of samples from the fits of auto-correlation curves by calibration prior to measurements as described in reference 25. The number of dyes per particle was measured by dividing particle concentration to concentration of free dye.

# CHAPTER 3

## RESULTS AND DISCUSSION

Main key factors over size and morphology control of ultra small SNPs are selecting TMOS as silica precursor, which hydrolyzes fast in water media, and using ammonium hydroxide as the base catalyst, which supports fast particle growth rate without any side effects on the particle morphology.<sup>16,17,20,22</sup> Introducing cationic micelle formation to this system results in porous nanoparticle morphology (mC-Dots) which is well studied in the literature.<sup>20</sup> Using hydrophobic TMB molecules as a micelle-swelling agent provides a larger pore size and forms a ring-shaped morphology (C-Rings), which has been recently reported by Ma et. al.<sup>21</sup>

Studying the nature of the morphology transition between these two particle geometries formed

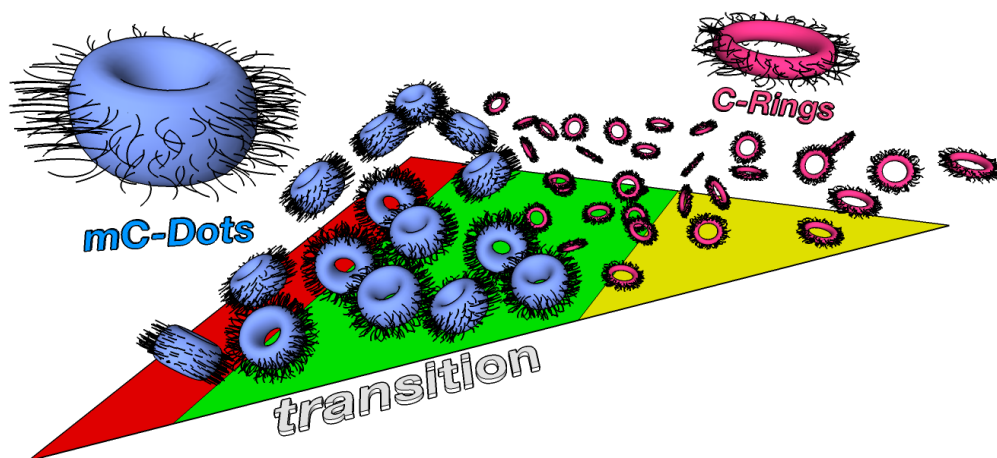


Fig. 3.1: Illustration of bimodal transition, and morphologies of mC-Dots and C-Rings. Red region shows the morphology before TMB addition. Green region is where transition occurs after the addition of TMB. Yellow region is where C-Rings' population size increases.

in similar synthesis conditions is essential in understanding oil/surfactant/silica interactions.

Here, we represent a bimodal transition between two different morphologies of porous SNPs: mC-Dots & C-Rings (Figure 3.1). Without any TMB addition, the morphology of the SNPs correspond to mC-Dots.<sup>17,20</sup> C-Rings formation starts with the addition of TMB. As the concentration of TMB increases, relative C-Rings population in the outcome of particles increases with decreasing relative mC-Dots population. When the TMB concentration is enough to swell all of the existing micelles in the batch<sup>24</sup>, the only particle outcome is C-Rings. Further TMB addition gets micelle sizes larger resulting in larger rings in terms of hydrodynamic diameter. Extra TMB addition does not get micelles any larger after the maximum average ring size is reached (Figure 3.2, Figure 5.2).<sup>24</sup>

This bimodal transition phenomenon was observed by FCS size measurements of different batches with varying TMB concentrations. Figure 3.2 shows the decrease of the average hydrodynamic size in the transition region. At 0 M TMB concentration, average size of mC-Dots population was measured to be 12.6 nm. The average size measured at 21.6 mM TMB concentration was 9.8 nm showing the decrease in size resulting from the formation of C-Rings population. At 61.3 mM TMB concentration, the minimum average size of 8.2 nm was measured. The decrease in the size from 12.6 nm to 8.2 nm shows the change in the relative number ratios of mC-Dots and C-Rings, since mC-Dots are hydrodynamically larger than C-Rings and biphasic nature of the transition gives the sum of these two populations.<sup>20,21</sup> Relative ratio of C-Rings population increases in the transition region resulting in the decrease in average size, until all of the particles formed are in ring geometry.

Further addition of TMB results in larger ring sizes (Figure 3.2, 5.3). Maximum average size (9.4 nm) of C-Rings was reached around 122.7 mM TMB concentration, and no significant change was observed between 122.7 mM and 360 mM TMB concentrations. DLS measurements of the batches with varying TMB concentrations also verified the size decrease in the transition region

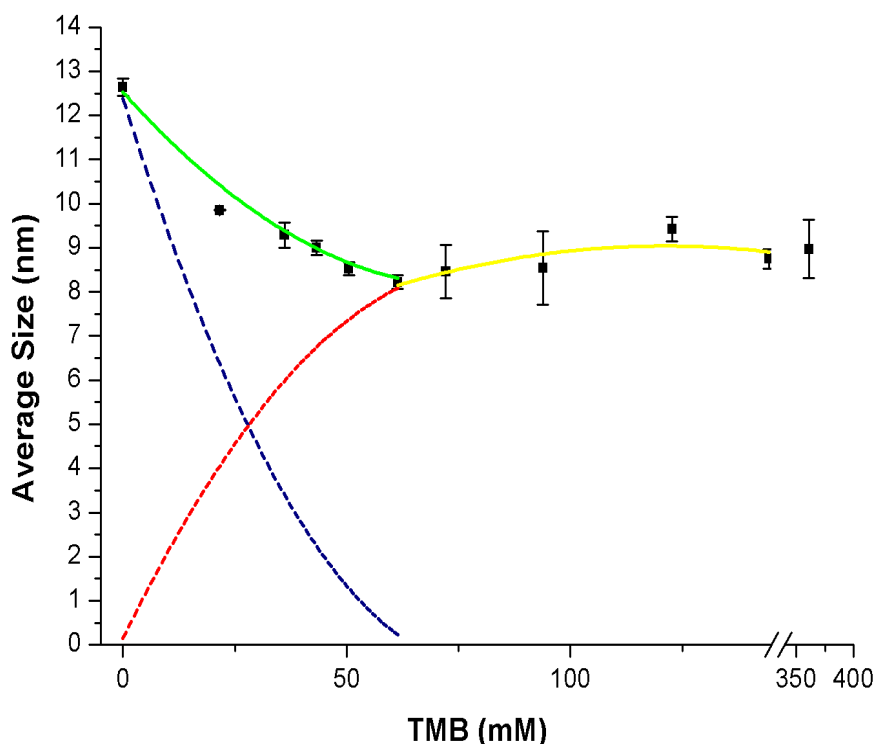


Fig. 3.2: Change in the hydrodynamic diameter of the samples (y-axis) upon the addition of TMB (x-axis) measured by FCS. Blue dotted line (mC-Dots) and red dotted line (C-Rings) fitted from the population ratios obtained by TEM analysis show the routes for extinction of mC-Dots and emergence of C-Rings. Green line, the cumulative weight of blue and red lines, shows the transition region route. Yellow line fitted from the FCS data showed by black squares is the region where C-Rings population's average size increases. All of the fits are 2<sup>nd</sup> degree polynomials. Error bars were calculated from reproduction of the samples for two times.

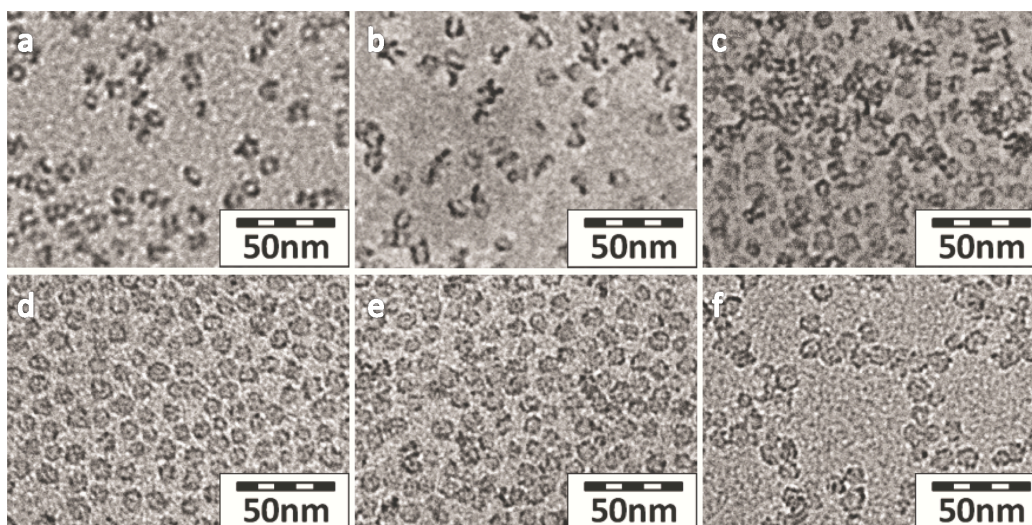


Fig. 3.3: TEM images at varying TMB concentrations: (a) 0 mM, (b) 14.4 mM, (c) 36 mM, (d) 54.1 mM, (e) 72.17 mM and (f) 144.35 mM. (b), (c) and (d) cover the transition region, whereas (a) contains only mC-Dots and (e) and (f) contains C-Rings at growth region.

and size increase of C-Rings with additional TMB (Figure 5.2). DLS measurements of the particles gave slightly small sizes relative to FCS measurements, since FCS only measures the size of the particles with fluorescent dyes.

TEM images of different batches with varying TMB concentrations verified the biphasic transition phenomena (Figure 3.3). In Figure 3.3a, star-shaped, one pore and half pore mC-Dots were observed at 0 mM TMB concentration. At 14.1 mM TMB concentration, C-Rings formation was observed (Figure 3.3b). Increase in the number of C-Rings was noticed at 36 mM TMB concentration (Figure 3.3c). Rings always are in torus shape, while mC-Dots tend to form star-shape, half, single and several pores morphology, but it is also possible to distinguish C-Rings from mC-Dots with the contrast difference (Figure 5.4).<sup>20,21</sup> At 54.1 mM TMB concentration, particles were predominantly C-Rings (Figure 3.3d).

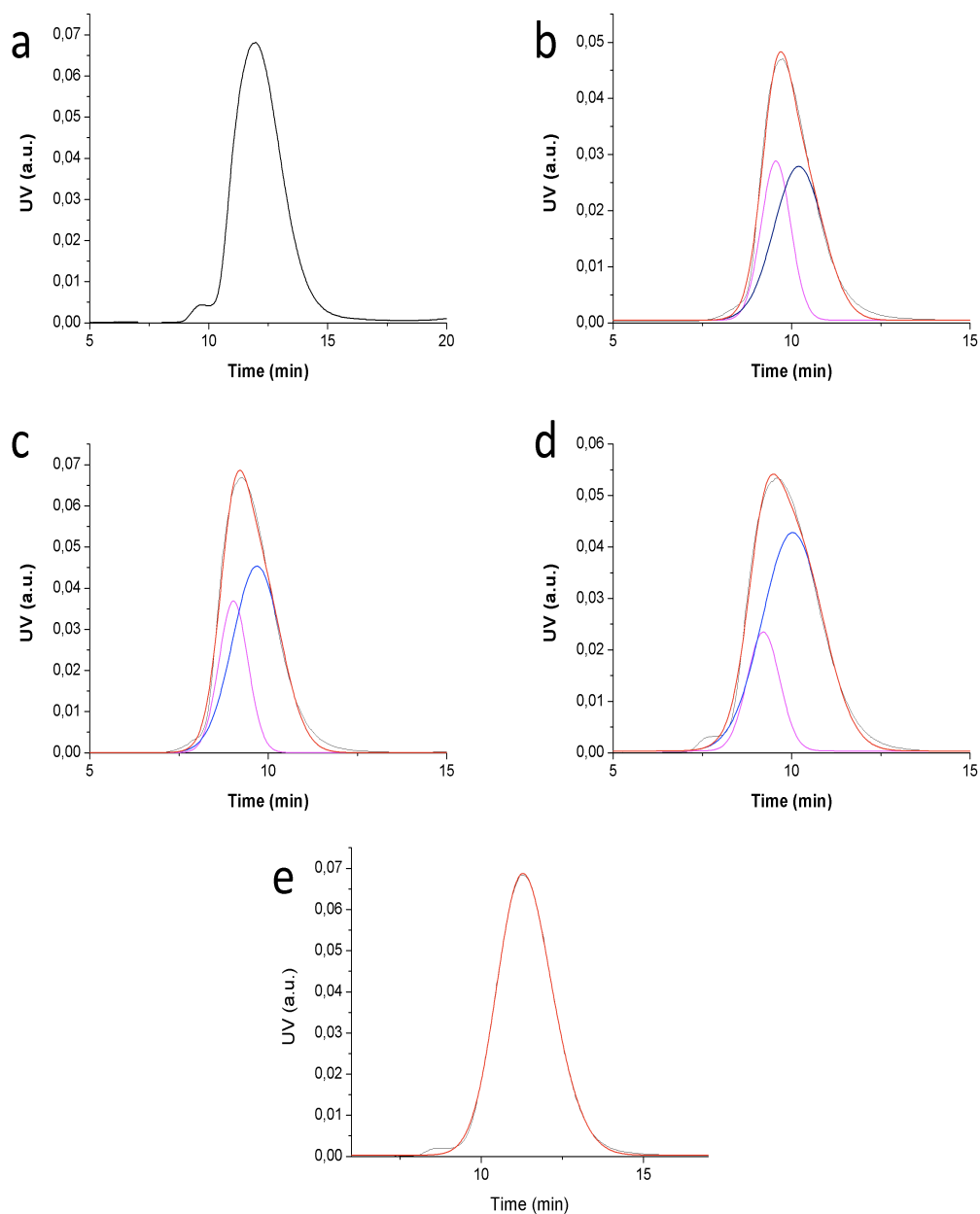


Fig. 3.4: Gaussian distributions for the GPC curves of the samples with varying TMB concentrations: (a) 0 mM, (b) 21,6 mM, (c) 36 mM, (d) 43.3 mM and (e) 61.3 mM. Red lines were fitted onto original GPC curves. Pink curves stand for mC-Dots population and blue curves stand for C-Rings population. (x-axis: time (min), y-axis: (UV intensity)). Distributions become more skewed in the transition region (b, c, d).

All of the particles observed in Figure 3.3e at 72.1 mM TMB concentration are in ring geometry, and Figure 3.3f contains C-Rings with larger diameter. Particle sizes obtained from TEM images are slightly smaller than hydrodynamic sizes obtained by FCS, since organic PEG layer is not visible in TEM.<sup>35</sup> The manufacturer specified TEM resolution is 0.35 nm.

GPC curves of the samples with varying TMB concentrations also showed a distortion of symmetry in the transition region, which was recovered after the transition (Figure 5.1). Figure 3.4 shows the Gaussian fits of mC-Dots and C-Rings populations at 0 mM, 21.65mM, 43.3 mM and 61.3 mM TMB concentrations. Decrease in the total area below the pink curves represents the decrease of the mC-Dots population relative to C-Rings population showing increase in the total area under blue curves. Figure 3.5a shows the relative the ratio change of mC-Dots and C-Rings calculated from the areas under the fitted GPC curves. As can be seen from Figure 3.5a, mC-Dots population decrease and C-Rings population increase. In addition, the skewness of the GPC curves also increases in the transition region, and then decreases and stabilizes at higher TMB concentrations where the only particle morphology is C-Rings (Figure 3.5b).

Size and morphology analysis were performed on the TEM images of the samples with varying TMB concentrations. Figure 3.5c shows the population changes of mC- Dots and C-Rings in the transition region, which is consistent with GPC analysis. Each population's particle number and average sizes were analyzed and the results showed that individual population average sizes do not change in the transition region (Figure 3.5d).

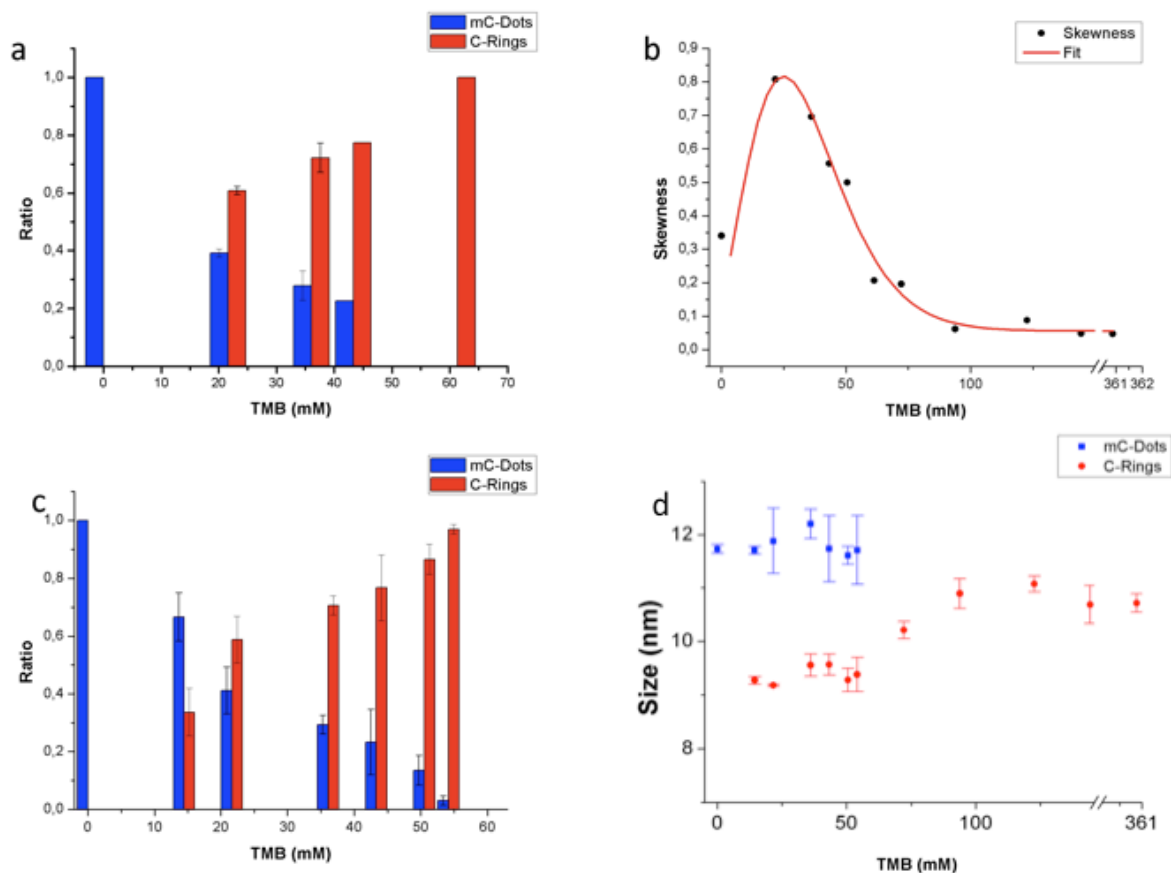


Fig. 3.5: Population ratios (a) of mC-Dots and C-Rings calculated from Gaussian fits of the GPC data, and Skewness (b) change of the samples (with Giddings fitting), TEM population ratio analysis (c) and TEM size analysis (d) at varying TMB concentrations. (a) and (c) show similar change mechanisms. (b) shows increasing skewness in the transition region. (d) shows that individual population sizes of mC-Dots and C-Rings stay constant in the transition region, whereas C-Rings' size increases afterwards.

MC-Dots have a constant average size in the transition region at different TMB concentrations. However, C-Rings population's average size increases in the growth region from 8.2 nm to 9.8 nm, and then reaches a fixed size around 9.5 nm, which is also consistent with the FCS data.

Assuming the mC-Dots and C-Rings populations' average sizes do not change in the transition region, we can actually calculate the relative ratios of each population from the average sizes of the whole samples measured by FCS. Figure 5.5 shows that this approximation gives a similar trend observed by the TEM analysis of ratios between the two populations.

Our results are also consistent with previous studies. Galarneau et. al. noted that they studied the window of  $0 < \text{TMB}/\text{C}_{16}\text{TAB} < 13$  (molar ratio) for oil/surfactant interactions, and found out that there are 3 steps in between the window<sup>24</sup>: the 1<sup>st</sup> is  $0 < \text{TMB}/\text{C}_{16}\text{TAB} < 1.6$ , where is almost no increase in micelle sizes.<sup>24</sup> In our system, there is a transition from mC-Dots to C-Rings with stable population sizes, until  $\text{TMB}/\text{C}_{16}\text{TAB}$  ratio is smaller than 2.6. In this step, at low TMB concentrations, absorption of TMB molecules by the micelle surfaces through cation- $\pi$  interactions could take place.<sup>12.14.14.15.24</sup>

Galarneau et. al. stated that in the 2<sup>nd</sup> step,  $1.6 < \text{TMB}/\text{C}_{16}\text{TAB} < 5$ , there is a fast growth of micelle sizes and in the 3<sup>rd</sup> one,  $\text{TMB}/\text{C}_{16}\text{TAB} > 5$ , micelle sizes do not change anymore<sup>24</sup>. In our case, C-Rings' micelle sizes increase in  $2.6 < \text{TMB}/\text{C}_{16}\text{TAB} < 5.3$  region through the swelling of micelles at higher TMB concentrations; and then C-Ring sizes stabilize at  $\text{TMB}/\text{C}_{16}\text{TAB} > 5.3$  region. Excess amounts of TMB results in more monodispersed distribution verified by the size skewness of the SNPs, consistent with previous studies that show that micelle distribution becomes more monodispersed at high TMB concentrations.<sup>24</sup>

Two scenarios can possibly lead to bimodal distribution in transition after the addition of TMB into micelle solution. 1) All of the micelles have the same size before the addition of TMOS, but

following the addition of TMOS some of the micelles get larger than others; and 2) Some of the micelles are larger than others before the addition of TMOS, and it does not change after the addition of TMOS. These two mechanisms may result in two different sizes of micelle populations leading to two distinct morphologies in the transition region.

Further investigations are required to understand the nature of oil/surfactant interactions resulting in the bimodal transition mechanism.

## CHAPTER 4

### CONCLUSION

In this study, we showed that there is a bimodal transition between mC-Dots and C-Rings upon the addition of TMB at varying concentrations. TEM analysis showed that the average sizes of mC-Dots and C-Rings are constant, but the population ratios reciprocally change in the transition region according to GPC, DLS, FCS and TEM data. MC-Dots' relative population ratio decreases until there is sufficient TMB for each micelle templating the formation of C-Rings. Upon the extinction of mC-Dots, additional TMB increases the particle sizes of C-Rings until the saturation of micelle cores by TMB.<sup>24</sup>

Bimodal morphology transition of MSNs (mC-Dots & C-Rings) is noteworthy to understand oil/surfactant interactions holding key for discovery of new types of materials for future applications, especially in bioimaging and drug delivery, where porous nature and morphology of the materials are essential.

# CHAPTER 5

## SUPPLEMENTAL MATERIALS

This section contains supporting figures of the thesis.

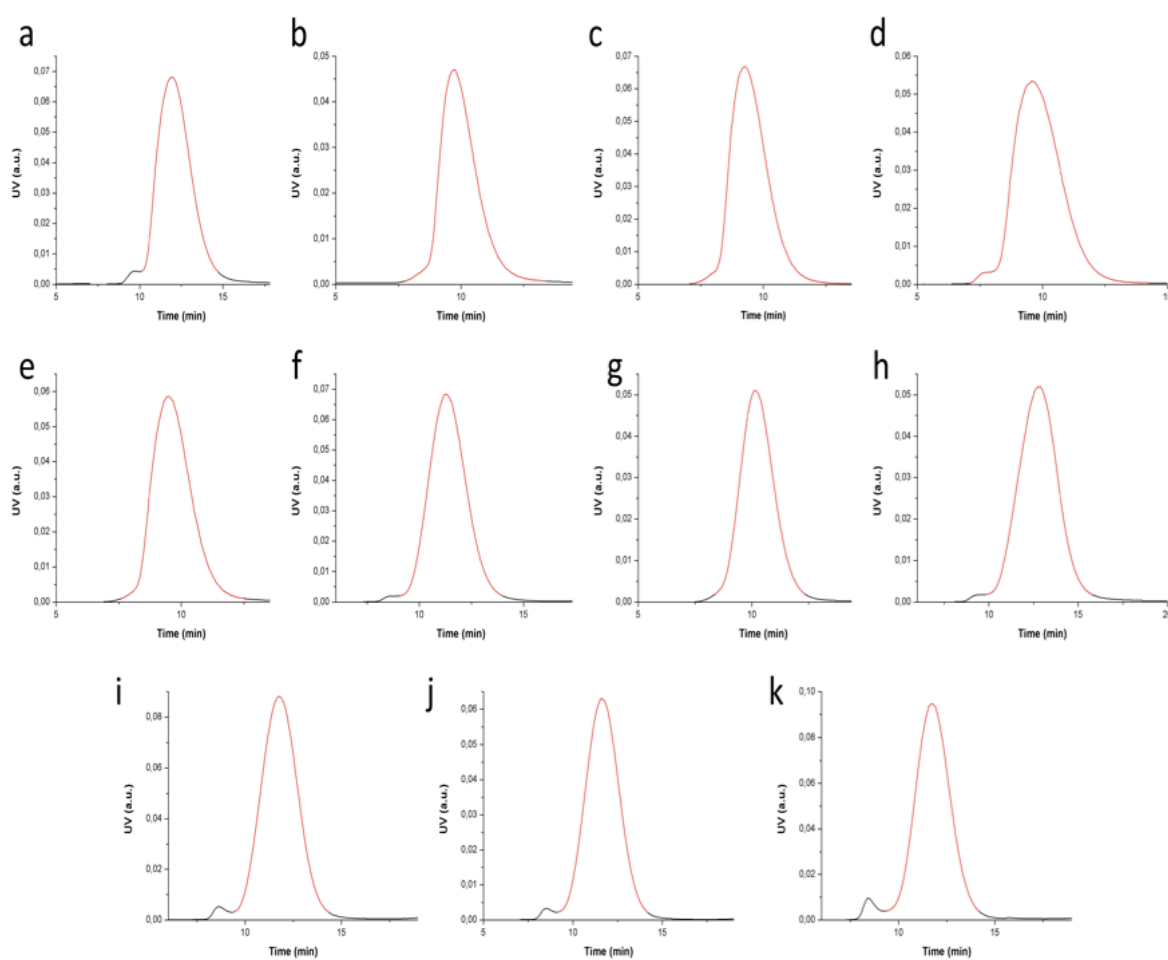


Fig. 5.1: GPC results of the samples with varying TMB concentrations: (a) 0 mM, (b) 21.6 mM, (c) 36 mM, (d) 43.3 mM, (e) 50.5 mM (f) 61.3 mM, (g) 72.17 mM, (h) 93.8 mM, (i) 122.7 mM, (j) 144.3 mM, (k) 360.8 mM. Skewness of curves increases in the transition region (b, c, d, e) and decreases later. Only the red curves were taken into consideration to avoid aggregation peaks.

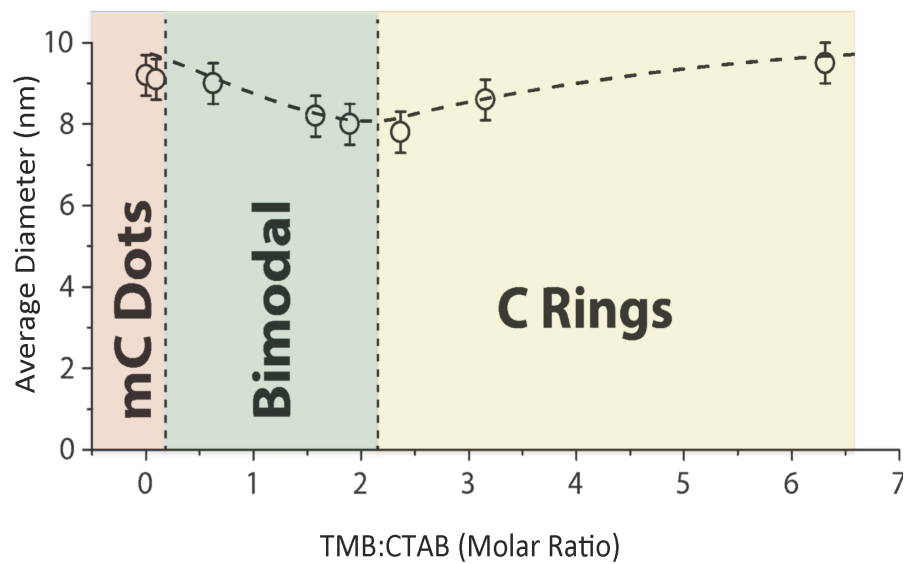


Fig. 5.2: Effect of varying TMB: CTAB ratio on hydrodynamic size measured by DLS for a fixed CTAB concentration. All of the particles are in mC-Dot morphology in red region. Green region is where transition occurs between two morphologies. Yellow region is the size growth region of C-Rings

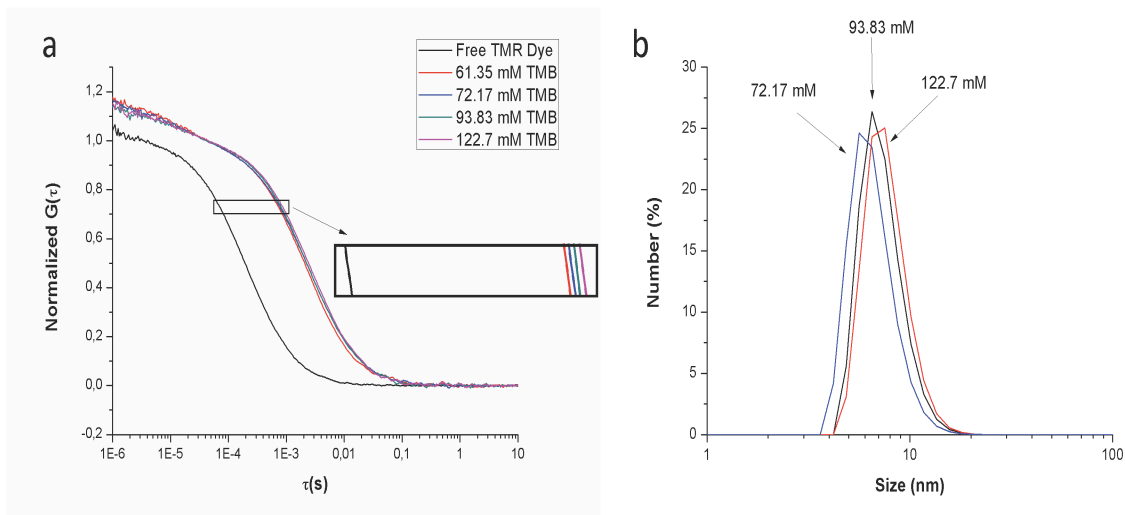


Fig. 5.3: Effect of varying TMB concentration increase on ring size in size growth region of C-Rings verified by FCS (a) and DLS (b) data

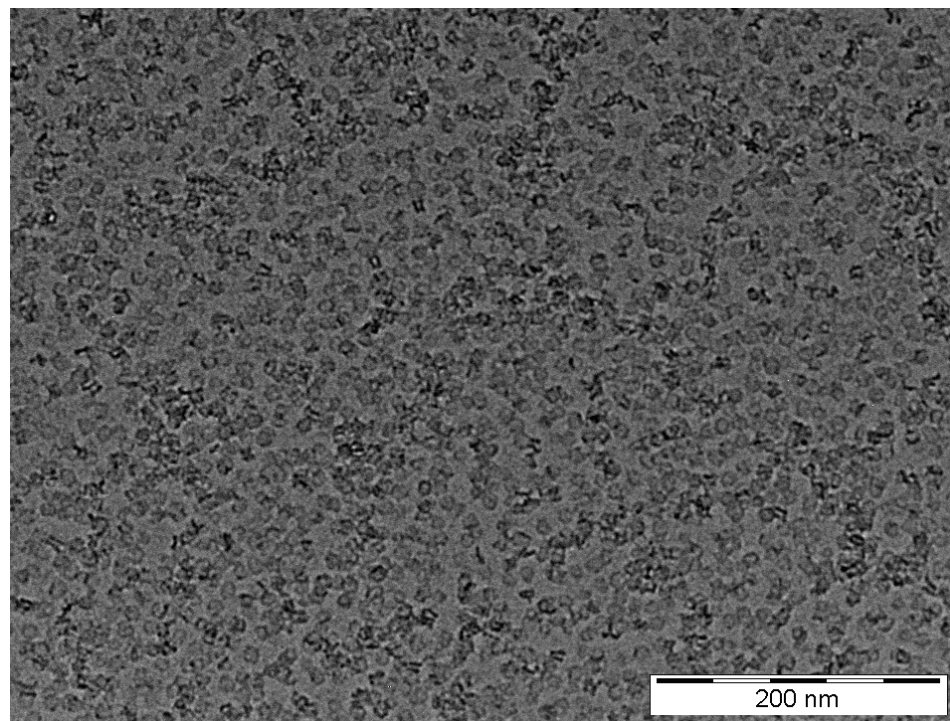


Fig. 5.4: TEM image of 43.3 mM TMB sample in transition region showing mC-Dots in darker and C-Rings in dimmer colors

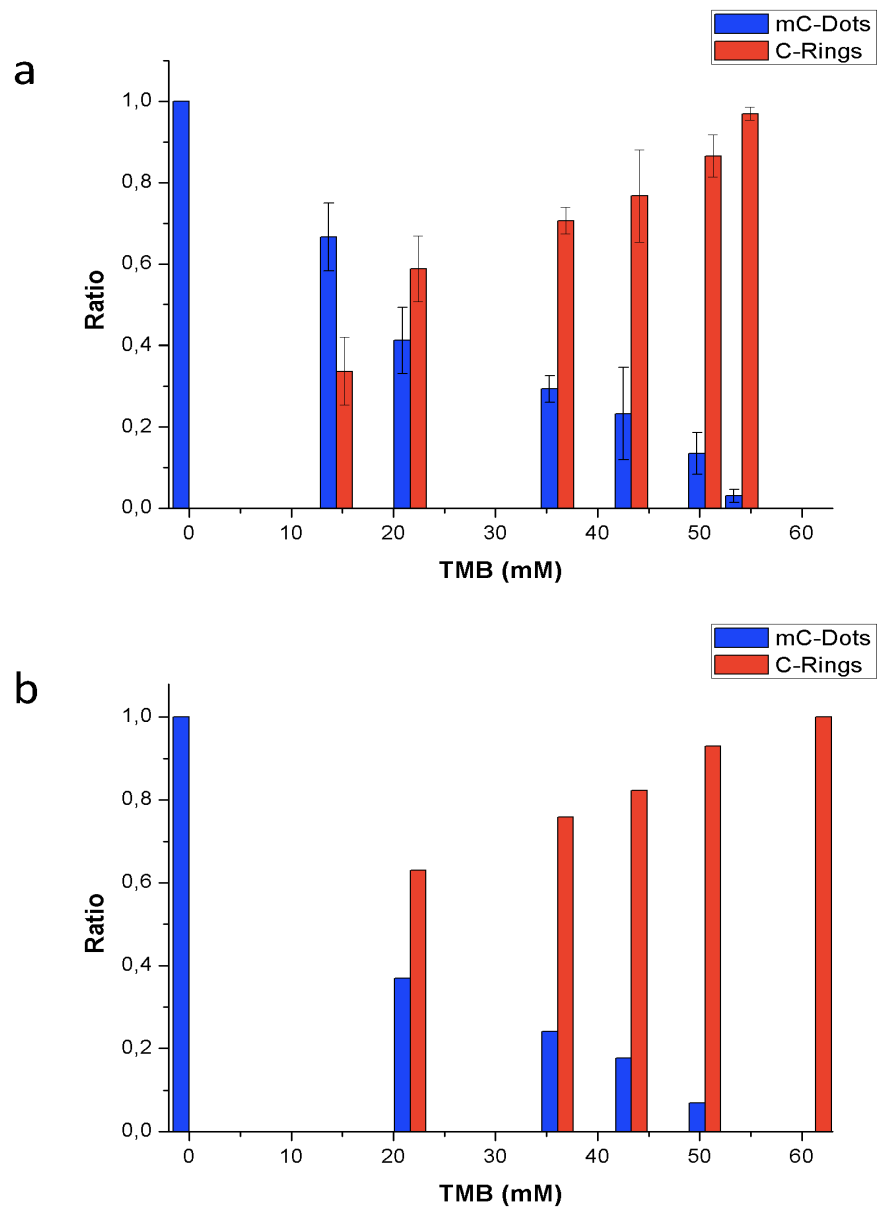


Fig. 5.5: Relative population ratios of mC-Dots (blue) and C-Rings (red) derived from TEM analysis (a) and calculation from the average sizes measured by FCS shows similar trends.

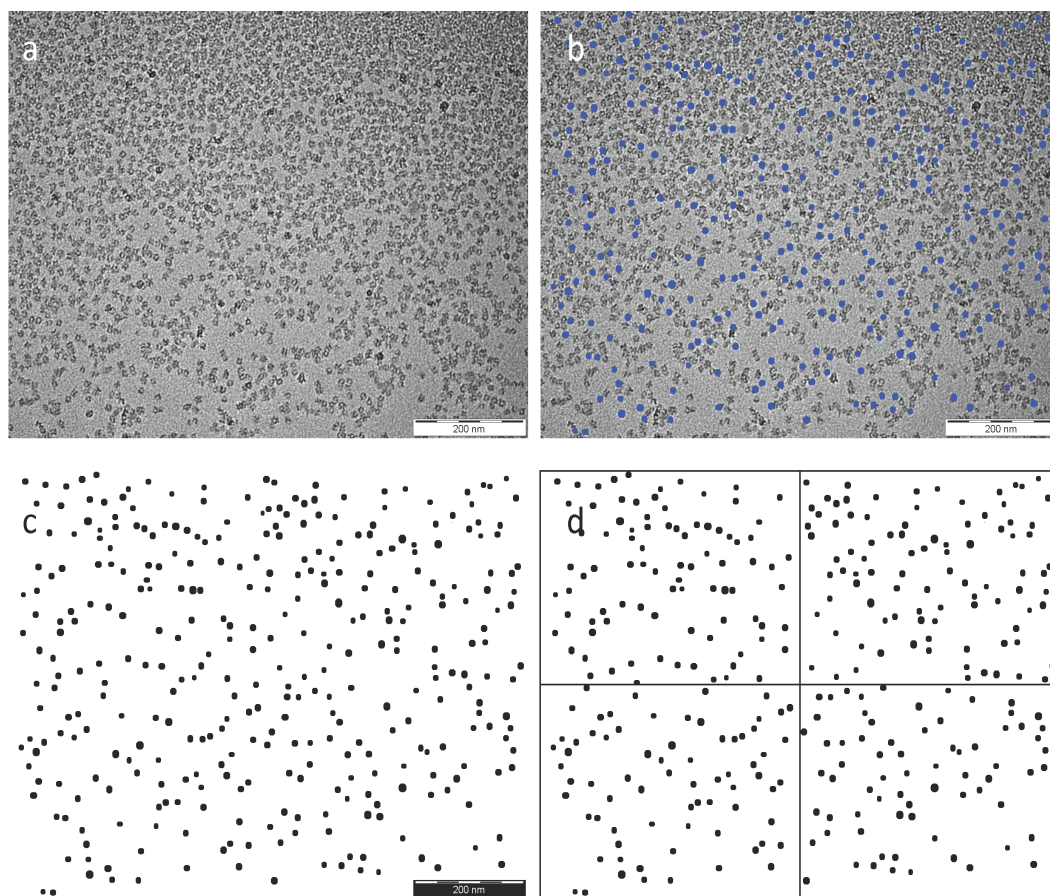


Fig. 5.6: TEM analysis of 0 mM TMB sample. (a) original image, (b) blue spheres drawn for mC-Dots, (c) image processing, (d) splitting for average size and error calculations.

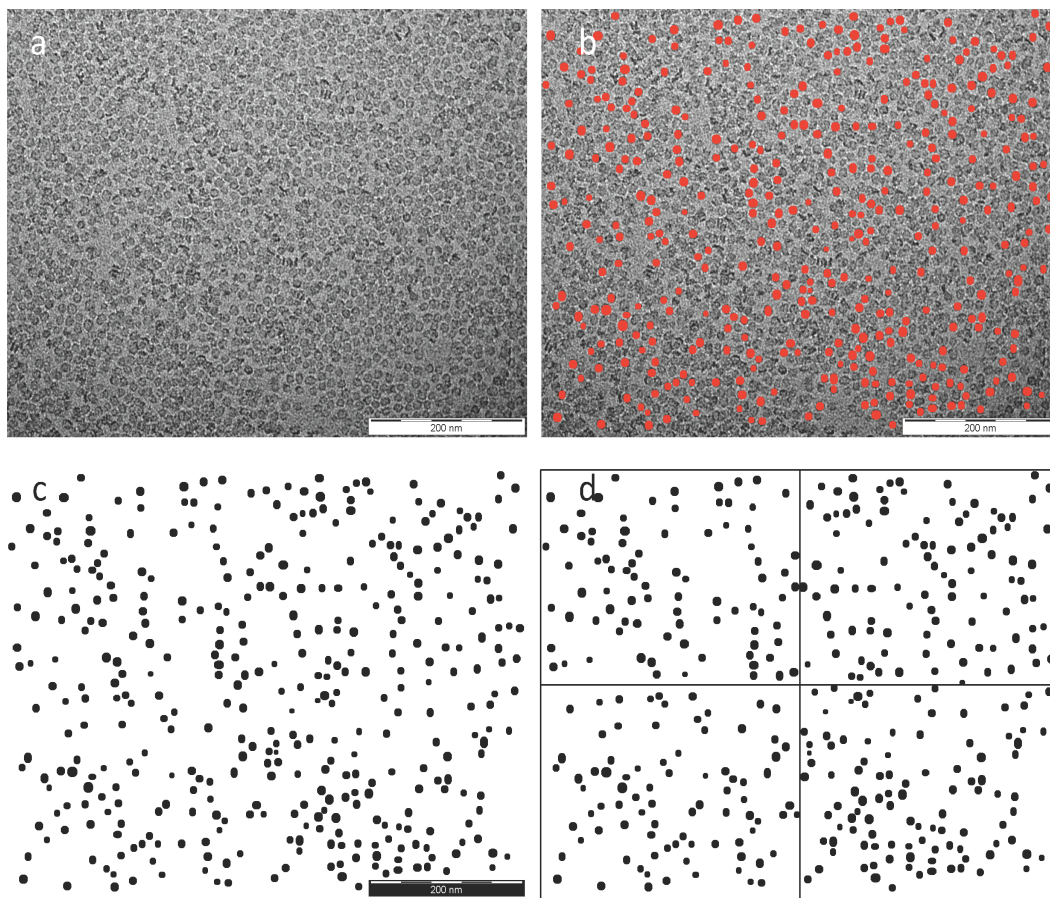


Fig. 5.7: TEM analysis of 72.17 mM TMB sample. (a) original image, (b) red spheres drawn for C-Rings, (c) image processing, (d) splitting for average size and error calculations.

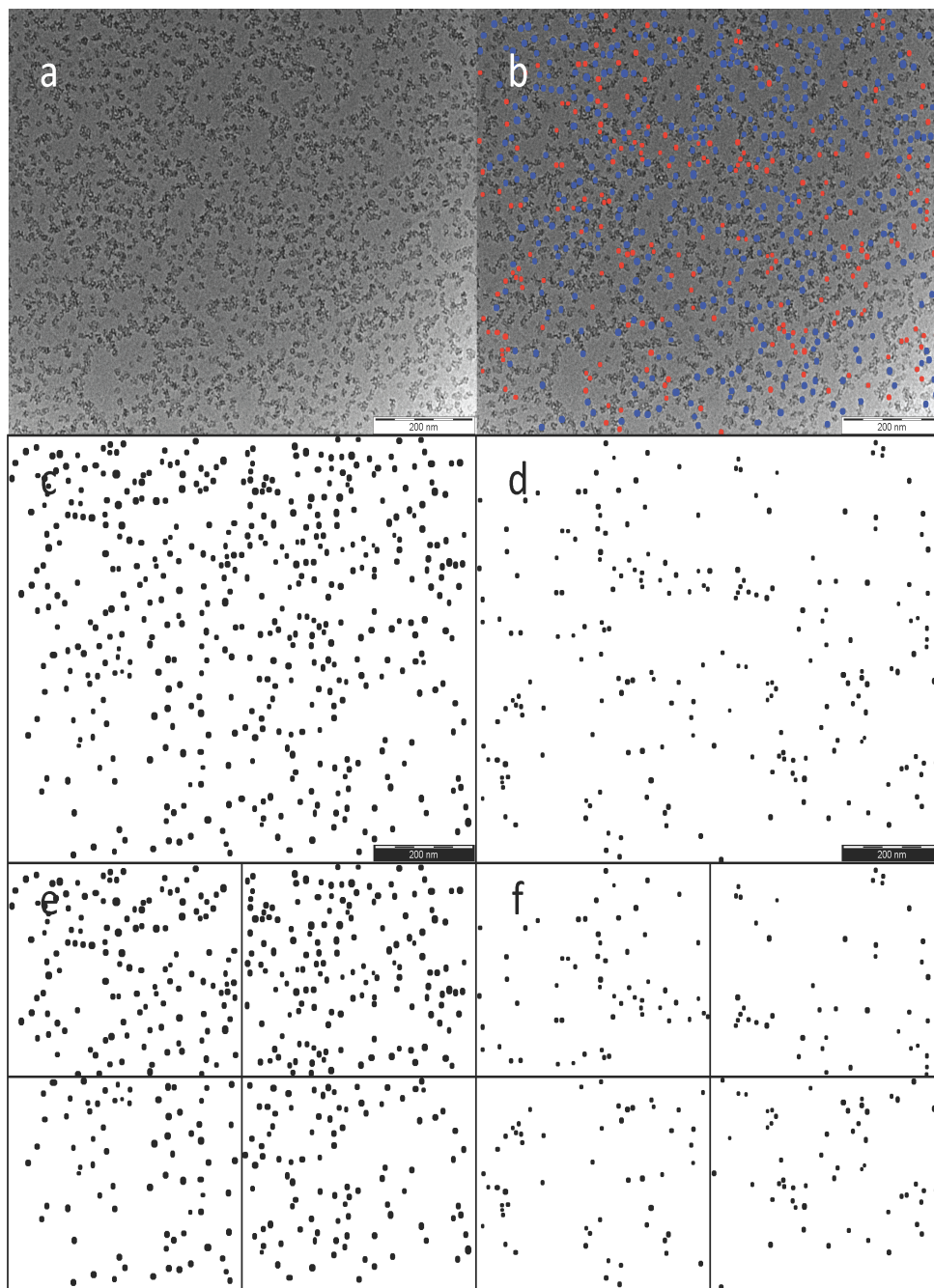


Fig. 5.8: TEM analysis of 14.43 mM TMB sample. (a) original image, (b) blue spheres drawn for mC-Dots, (c) image processing, (d) splitting for average size and error calculations.

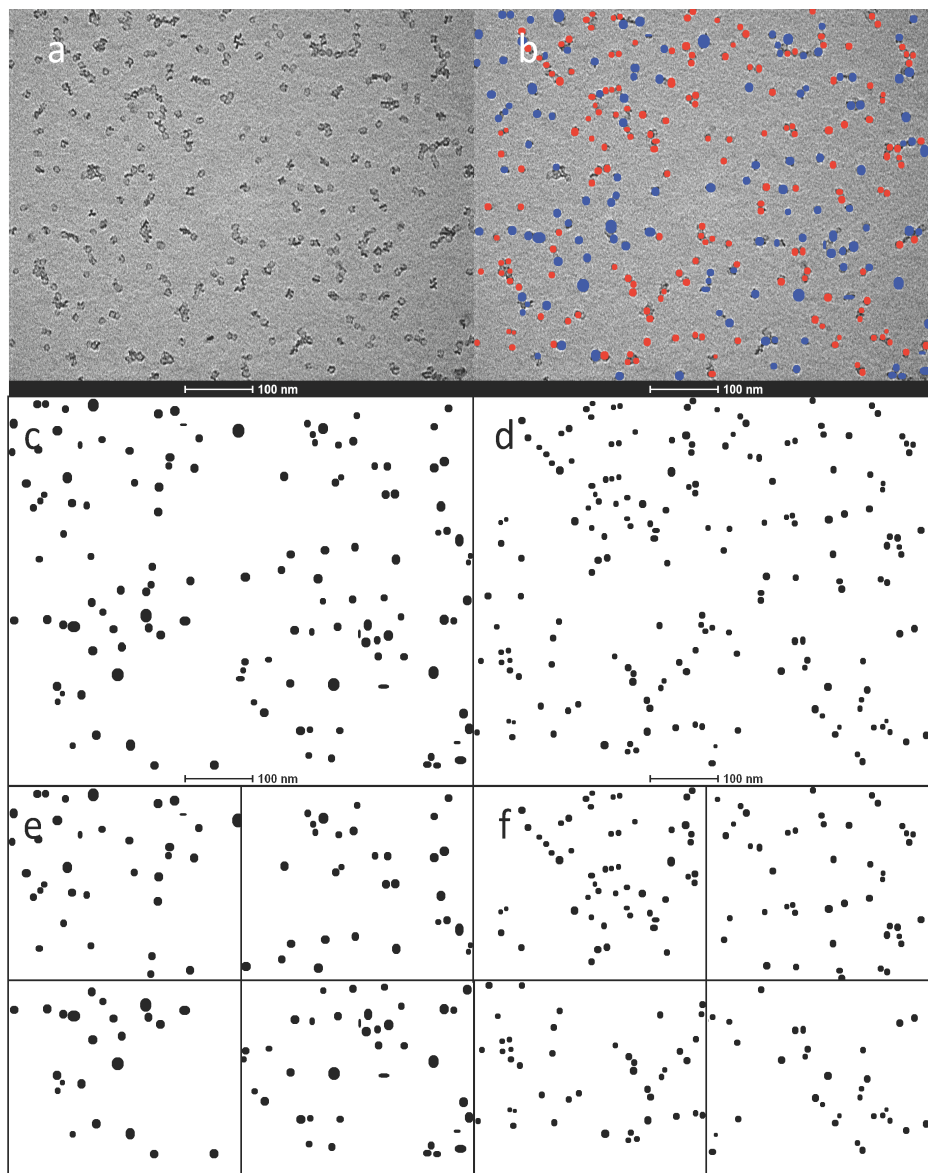


Fig. 5.9: TEM analysis of 21.65 mM TMB sample. (a) original image, (b) blue spheres drawn for mC-Dots, (c) image processing, (d) splitting for average size and error calculations.

TEM population size, and ratio analysis of mC-Dots were done by counting individual star shaped, half, single and several pore particles described in literature.<sup>17,20</sup> While C-Rings were distinguished from the larger and single pore size morphology and dimmer color on TEM image.

## REFERENCES

- [1] Kresge, C. T.; Leonowicz, M. E.; Roth, W. J.; Vartuli, J. C.; Beck, J. S. Ordered Mesoporous Molecular Sieves Synthesized by a Liquid-Crystal Template Mechanism. *Nature*, **1992**, *359*, 710–712.
- [2] Beck, J. S.; Vartuli, J. C.; Roth, W. J.; Leonowicz, M. E.; Kresge, C. T.; Schmitt, K. D.; Chu, C. T.-W.; Olson, D. H.; Sheppard, E. W.; McCullen, S. B.; et al. A New Family of Mesoporous Molecular Sieves Prepared with Liquid Crystal Templates. *J. Am. Chem. Soc.* **1992**, *114*, 10834–10843.
- [3] Zhao, D.; Feng, J.; Huo, Q.; Melosh, N.; Frederickson, G. H.; Chmelka, B. F.; Stucky, G. D. Triblock Copolymer Syntheses of Mesoporous Silica with Periodic 50 to 300 Angstrom Pores. *Science*. **1998**, *279*, 548–552.
- [4] Schmidt-Winkel, P.; Lukens, W. W.; Zhao, D.; Yang, P.; Chmelka, B. F.; Stucky, G. D. Mesocellular Siliceous Foams with Uniformly Sized Cells and Windows. *J. Am. Chem. Soc.* **1999**, *121*, 254–255.
- [5] Schmidt-Winkel, P.; Lukens, W. W.; Yang, P.; Margolese, D. I.; Lettow, J. S.; Ying, J. Y.; Stucky, G. D. Microemulsion Templating of Siliceous Mesostructured Cellular Foams with Well-Defined Ultralarge Mesopores. *Chem. Mater.* **2000**, *12*, 686–696.
- [6] Lettow, J. S.; Han, Y. J.; Schmidt-Winkel, P.; Yang, P. D.; Zhao, D. Y.; Stucky, G. D.; Ying, J. Y. Hexagonal to Mesocellular Foam Phase Transition in Polymer- Templated Mesoporous Silicas. *Langmuir* **2000**, *16*, 8291–8295.
- [7] Wang, T.; Chen, D.; Ma, J.; Wen, S.; Liu, Q. Synthesis and Characterisation of Pore-Expanded Mesoporous Silica Materials. *Micro Nano Lett.* **2015**, *10*, 140–144.
- [8] Monnier, a; Schüth, F.; Huo, Q.; Kumar, D.; Margolese, D.; Maxwell, R. S.; Stucky, G. D.; Krishnamurty, M.; Petroff, P.; Firouzi, a; et al. Cooperative Formation of Inorganic-Organic Interfaces in the Synthesis of Silicate Mesostructures. *Science* **1993**, *261*, 1299–1303.
- [9] Firouzi, A.; Kumar, D.; Bull, L. M.; Besier, T.; Sieger, P.; Huo, Q.; Walker, S. a; Zasadzinski, J. A.; Glinka, C.; Nicol, J.; et al. Cooperative Organization of Inorganic-Surfactant and Biomimetic Assemblies. *Science* **1995**, *267*, 1138–1143.
- [10] Aveyard, R.; Binks, B. P.; Cooper, P.; Fletcher, P. D. I. Mixing of Oils with Surfactant Monolayers. *Progr Colloid Polym Sci* **1990**, *40*, 36–40.

- [11] Nelson, P. H.; Hatton, T. A.; Rutledge, G. C. Asymmetric Growth in Micelles Containing Oil. *Chem. Phys.* **1999**, *110*.
- [12] Blin, J. L.; Su, B. L. Tailoring Pore Size of Ordered Mesoporous Silicas Using One or Two Organic Auxiliaries as Expanders. *Langmuir* **2002**, *18*, 5303–5308.
- [13] Ottaviani, M. F.; Moscatelli, A.; Desplandier-Giscard, D.; Renzo, F. D.; Kooyman, P. J.; Alonso, B.; Galarneau, A. Synthesis of Micelle-Templated Silicas from Cetyltrimethylammonium Bromide / 1, 3, 5-Trimethylbenzene. *J. Phys. Chem. B* **2004**, *108*, 12123–12129.
- [14] Jiang, D.; Gao, J.; Li, J.; Yang, Q.; Li, C. Structural Control of Mesoporous Ethane-Silicas with Trans-(1R,2R)-Diaminocyclohexane in the Pore and Asymmetric Catalysis. *Microporous Mesoporous Mater.* **2008**, *113*, 385–392.
- [15] Eriksson, J. C.; Gillberg, G.; Røst, E.; Vestersjø, E.; Stokke, O.; Bunnberg, E.; Djerassi, C.; Records, R. NMR-Studies of the Solubilisation of Aromatic Compounds in Cetyltrimethylammonium Bromide Solution. II. *Acta Chemica Scandinavica*, **1966**, *20*, 2019–2027.
- [16] Wang, J.; Sugawara-Narutaki, A.; Fukao, M.; Yokoi, T.; Shimojima, A.; Okubo, T. Two-Phase Synthesis of Monodisperse Silica Nanospheres with Amines or Ammonia Catalyst and Their Controlled Self-Assembly. *ACS Appl. Mater. Interfaces* **2011**, *3*, 1538–1544.
- [17] Ma, K.; Sai, H.; Wiesner, U. Ultrasmall Sub-10 Nm Near-Infrared Fluorescent Mesoporous Silica Nanoparticles. *J. Am. Chem. Soc.* **2012**, *134*, 13180–13183.
- [18] Phillips, E.; Penate-Medina, O.; Zanzonico, P. B.; Carvajal, R. D.; Mohan, P.; Ye, Y.; Humm, J.; Gonen, M.; Kalaigian, H.; Schoder, H.; *et al.* Clinical Translation of an Ultrasmall Inorganic Optical-PET Imaging Nanoparticle Probe. *Sci. Transl. Med.* **2014**, *6*, 260, 1-9.
- [19] Jiang, D.; Gao, J.; Li, J.; Yang, Q.; Li, C. Structural Control of Mesoporous Ethane-Silicas with Trans-(1R,2R)-Diaminocyclohexane in the Pore and Asymmetric Catalysis. *Microporous Mesoporous Mater.* **2008**, *113*, 385–392.
- [20] Ma, K.; Werner-Zwanziger, U.; Zwanziger, J.; Wiesner, U. Controlling Growth of Ultrasmall Sub-10 Nm Fluorescent Mesoporous Silica Nanoparticles. *Chem. Mater.* **2013**, *25*, 677–691.
- [21] Ma, K. *et al.* C-Rings Paper, *in preparation*.
- [22] Brinker, C. J.; Scherer, G. W.; *Sol-Gel Science: The Physics and Chemistry of Sol-Gel Processing*; Academic Press, Inc.; San Diego, CA, **1990**.

- [23] Stöber, W.; Fink, A.; Bohn, E. Controlled Growth of Monodisperse Silica Spheres in the Micron Size Range. *J. Colloid Interface Sci.* **1968**, *26*, 62–69.
- [24] Lefèvre, B.; Galarneau, a.; Iapichella, J.; Petitto, C.; Di Renzo, F.; Fajula, F.; Bayram-Hahn, Z.; Skudas, R.; Unger, K. Synthesis of Large-Pore Mesostructured Micelle-Templated Silicas as Discrete Spheres, *Chem. Mater.* **2005**, *17*, 601–607.
- [25] Larson, D. R.; Ow, H.; Vishwasrao, H. D.; Heikal, A. a; Wiesner, U.; Webb, W. W. Silica Nanoparticle Architecture Determines Radiative Properties of Encapsulated Fluorophores. *Chem. Mater.*, **2008**, *20*, 2677–2684.
- [26] Ruppert, D.; Statistics and Data Analysis for Financial Engineering; Springer; New York, **2010**.
- [28] Mal, N. K.; Fujiwara, M.; Tanaka, Y. Photocontrolled Reversible Release of Guest Molecules from Coumarin- Modified Mesoporous Silica. *Nature* **2003**, *421*, 350–353.
- [29] Slowing, I. I.; Vivero-Escoto, J. L.; Wu, C.-W.; Lin, V. S.-Y. Mesoporous Silica Nanoparticles as Controlled Release Drug Delivery and Gene Transfection Carriers. *Adv. Drug Deliv. Rev.* **2008**, *60*, 1278–1288.
- [30] Vallet-Regí, M.; Balas, F.; Arcos, D. Mesoporous Materials for Drug Delivery. *Angew. Chemie - Int. Ed.* **2007**, *46*, 7548–7558.
- [31] Tang, F.; Li, L.; Chen, D. Mesoporous Silica Nanoparticles: Synthesis, Biocompatibility and Drug Delivery. *Adv. Mater.* **2012**, *24*, 1504–1534.
- [32] Liu, J.; Bu, W.; Pan, L.; Shi, J. NIR-Triggered Anticancer Drug Delivery by Upconverting Nanoparticles with Integrated Azobenzene-Modified Mesoporous Silica. *Angew. Chemie - Int. Ed.* **2013**, *52*, 4375–4379.
- [33] Trewyn, B. G.; Whitman, C. M.; Lin, V. S.-Y. Morphological Control of Room-Temperature Ionic Liquid Templated Mesoporous Silica Nanoparticles for Controlled Release of Antibacterial Agents. *Nano Lett.* **2004**, *4*, 2139–2143.
- [34] Slowing, I. I.; Trewyn, B. G.; Giri, S.; Lin, V. S. Y. Mesoporous Silica Nanoparticles for Drug Delivery and Biosensing Applications. *Adv. Funct. Mater.* **2007**, *17*, 1225–1236.
- [35] Sun, Y.; Sai, H.; von Stein, F.; Riccio, M.; Wiesner, U. Water-Based Synthesis of Ultrasmall PEGylated Gold-Silica Core-Shell Nanoparticles with Long-Term Stability. *Chem. Mater.*, **2014**, *26*, 5201–5207.